Single-molecule imaging reveals the kinetics of non-homologous end-joining in living cells

Mariia Mikhova[1,2], **Joshua R. Heyza**[2], **Katheryn Meek**[3,4], **and Jens C. Schmidt**[2,5,✉]

[1]Department of Biochemistry and Molecular Biology, Michigan State University, East Lansing, MI, U.S.A.
[2]Institute for Quantitative Health Sciences and Engineering, Michigan State University, East Lansing, MI, U.S.A.
[3]Department of Microbiology and Molecular Genetics, Michigan State University, East Lansing, MI, U.S.A.
[4]Department of Pathobiology Diagnostic Investigation, Michigan State University, East Lansing, MI, U.S.A.
[5]Department of Obstetrics, Gynecology, and Reproductive Biology, Michigan State University, East Lansing MI, U.S.A.

Non-homologous end joining (NHEJ) is the predominant pathway that repairs DNA double-stranded breaks (DSBs) in vertebrates. The DNA termini of many DSBs must be processed to allow ligation while minimizing genetic changes that result from break repair. Emerging models propose that DNA termini are first synapsed approximately 115Å apart in one of two long-range synaptic complexes. The first long-range complex can be formed with only the KU70/80 heterodimer and DNA-PKcs while the second long-range complex also includes XRCC4, XLF, and Ligase 4. Both long-range complexes inefficiently progress to short-range synaptic complexes that juxtapose DNA ends to facilitate ligation. Here we perform single-molecule analyses of the recruitment of Halo-tagged NHEJ factors to DSBs. Our results provide direct evidence for stepwise maturation of NHEJ complex and precisely define kinetics of core NHEJ factor binding to DSBs in living cells.

DNA repair | Non-homologous end joining | Single-molecule imaging | DNA-PKcs | Genome Stability

Correspondence:
schmi706@msu.edu (Twitter: @jenscs83)

Introduction

DNA, the blue-print of life, is remarkably labile and can be damaged in a variety of ways. Damage that results in DNA double strand breaks (DNA breaks on both strands, DSBs) is the most toxic genomic lesion [1–3]. DSBs that are left unrepaired or repaired incorrectly can result in mutations or loss of genetic information due to chromosomal rearrangements, and in some cases cell death. Two major DNA double-strand break repair pathways are present in most organisms [1–3]. Non-homologous end-joining (NHEJ) directly ligates DNA ends after limited end-processing to render DNA ends chemically compatible for ligation [2]. NHEJ is active throughout the cell cycle and is estimated to repair 80% of all spontaneous DSBs in human cells [4]. Homologous recombination (HR) utilizes a sister chromatid to serve as a template DNA to repair DSBs [5]. Due to the requirement for a sister chromatid, HR functions only in the S and G2 phases of the cell cycle.

The core NHEJ factors include Ku70, Ku80, DNA-PKcs, XLF, XRCC4 and Lig4 [2]. The highly abundant heterodimer of Ku70 and Ku80 (Ku70/80) forms a ring structure that binds double-stranded DNA ends with a high affinity [6]. Ku70/80 serves as the regulatory subunit of the DNA-dependent protein kinase (DNA-PK), which is activated when Ku70/80 binds DNA ends, resulting in recruitment of DNA-PKcs, the catalytic subunit of DNA-PK [7]. Ku70/80, and to a lesser extent DNA-PKcs, serve as a scaffold to target the other core NHEJ factors as well as numerous end-processing enzymes, many of which possess Ku-binding motifs that facilitate assembly of various NHEJ complexes [6,8].

In recent years, cryogenic electron microscopy (Cryo-EM), and in vitro single-molecule imaging studies have significantly advanced our understanding of the assembly mechanism underlying the recruitment of the core NHEJ factors to facilitate DSB repair [9–15]. Elegant single-molecule Förster resonance energy transfer (FRET) studies suggest that after Ku70/80 binds DNA ends and recruits DNA-PKcs, the DNA ends are synapsed, but are positioned more than 100 Å apart in a long-range synaptic complex [14,15]. This long-range complex can progress into a short-range synaptic complex where the ends are in sufficiently close proximity to facilitate ligation. This transition requires Ku70/80, the catalytic activity of DNA-PKcs, and components of the ligase complex (Lig4, XRCC4, and XLF) [15]. Recently a plethora of new Cryo-EM studies have provided support for this model and surprisingly defined two distinct long-range complexes, one exclusively mediated by Ku70/80 and DNA-PKcs and a second long-range complex that also includes XLF, XRCC4 and Lig4 [9–13]. Follow-up mutational experiments suggested that the long-range complexes facilitate distinct end-processing reactions that are required for the repair of DSBs with specific DNA end chemistries [16]. Importantly, we currently lack direct evidence for the existence of different NHEJ complexes in cells and a clear understanding of the timing and progression of NHEJ in vivo. In this study, we use single-molecule imaging of endogenously HaloTagged DNA repair factors to analyze the kinetics of NHEJ in living cells. We define the recruitment dynamics of the core NHEJ factors to DSBs and show that repair of a DSB in human cancer cell line by NHEJ takes approximately 30 minutes. Our results demonstrate that Ku70/80 and DNA-PKcs are recruited to DSBs before the components of the ligase complex (XRCC4, XLF, Lig4), consistent with the formation of a long-range complex that only contains Ku70/80 and DNA-PKcs. In addition, we observe that DNA-PKcs dissociates from DSBs 10 minutes prior to Ku70/80, XLF, and XRCC4. The dissociation of DNA-PKcs represents the progression of the long-

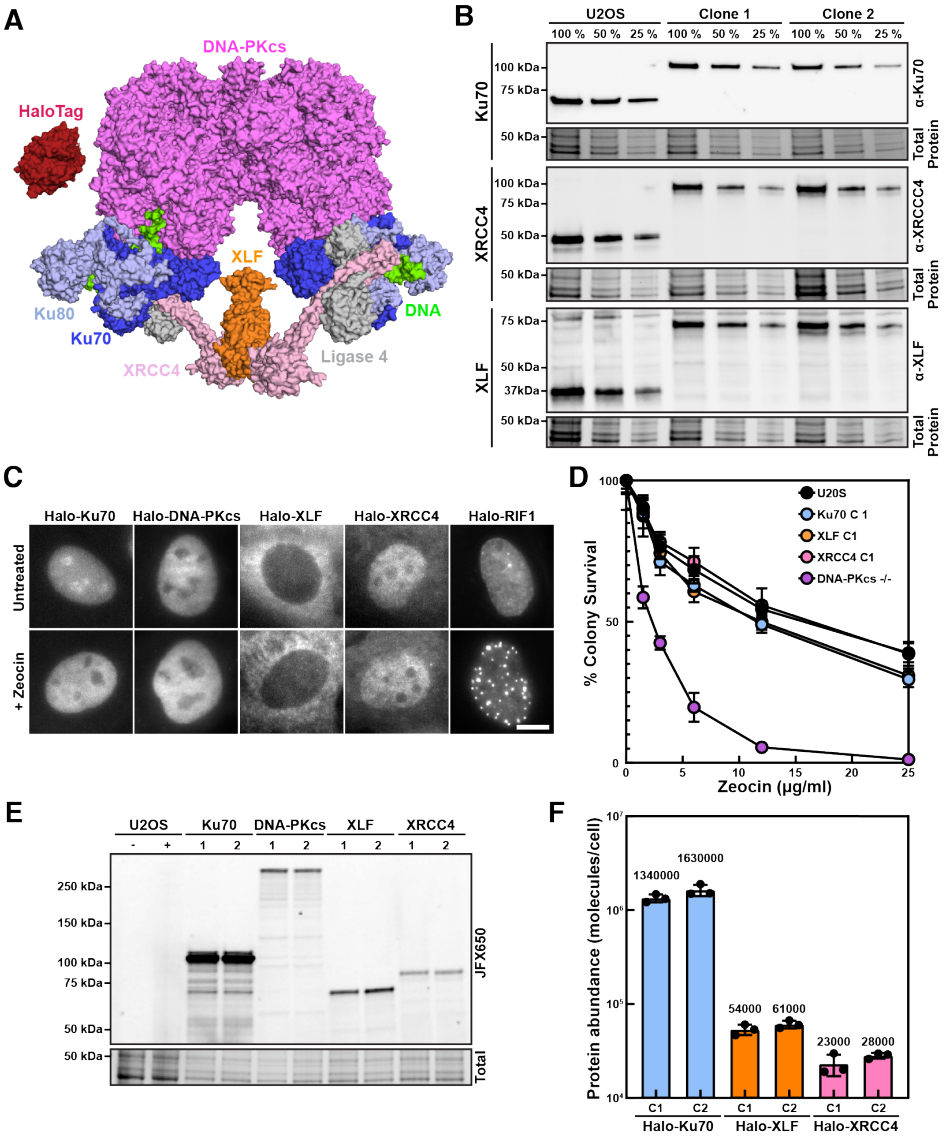

Fig. 1. Generation and validation of HaloTagged core NHEJ proteins in U20S cells. A Graphical depiction of the long-range XLF-mediated NHEJ synaptic complex and HaloTag (based on PDB: 7NFC and 6U32) [13,44]. **B** Western blots of U2OS cells expressing HaloTagged NHEJ factors and parental U2OS cells probed with antibodies against Ku70 (top), XRCC4 (middle), and XLF (bottom). **C** Representative images of living cells expressing HaloTagged NHEJ factors and Halo-Rif1 labeled with JFX650 HaloTag ligand in the presence or absence of Zeocin (Scale bar = 10 um). **D** Clonogenic survival assay of U2OS cells expressing HaloTagged NHEJ factors, parental U2OS cells, and U2OS cells with DNA-PKcs knocked out after challenge with Zeocin (N = 4, 3 technical replicates per biological replicate, Mean ± S.D.). **E** Fluorescence imaging of 2 clones of each HaloTagged NHEJ factor labeled with JF650 HaloTag ligand and separated on an SDS-PAGE gel. **F** Quantification of the total protein abundance based on recombinant 3X FLAG-HaloTag labeled with JF646 and cell lysates from a specific number of U2OS using in-gel fluorescence intensity values after applying a correction factor from western blots (see Fig. S1C-D, N = 3, Mean ± S.D.).

range synaptic NHEJ complex to the short-range synaptic complex as first proposed by Graham et al. and visualized recently in Cryo-EM structures of NHEJ complexes [11–13,15]. Importantly, the dissociation of DNA-PKcs requires its catalytic activity, and its inhibition also prevents the release of all other NHEJ factors analyzed. Altogether our work provides direct evidence for the existence of NHEJ complexes with distinct compositions in living cells and precisely determines their maturation over time to define the kinetics of non-homologous end joining *in vivo*.

Results

Generation of functional, endogenously HaloTagged NHEJ factors. To facilitate live cell single-molecule imaging of NHEJ factors, CRISPR-Cas9 and homology-directed repair were used to insert the coding sequence for a 3xFLAG-HaloTag (Halo) at the N-terminus of the endogenous loci encoding Ku70, DNA-PKcs (generated in our previous work [17]), XLF, and XRCC4 in U2OS cells (Fig. 1A). For each gene, all alleles were edited; the insertions were verified using Sanger sequencing, and exclusive expression of the tagged protein was confirmed using western blot (Fig. 1B). To assess subcellular localization of the HaloTagged NHEJ factors, cells were labeled with a fluorescent HaloTag ligand (JFX650), and the tagged proteins were visualized using widefield fluorescence microscopy. In the presence or absence of the DSB-inducing drug Zeocin, Halo-Ku70, Halo-DNA-PKcs, and Halo-XRCC4 localize exclusively to the nu-

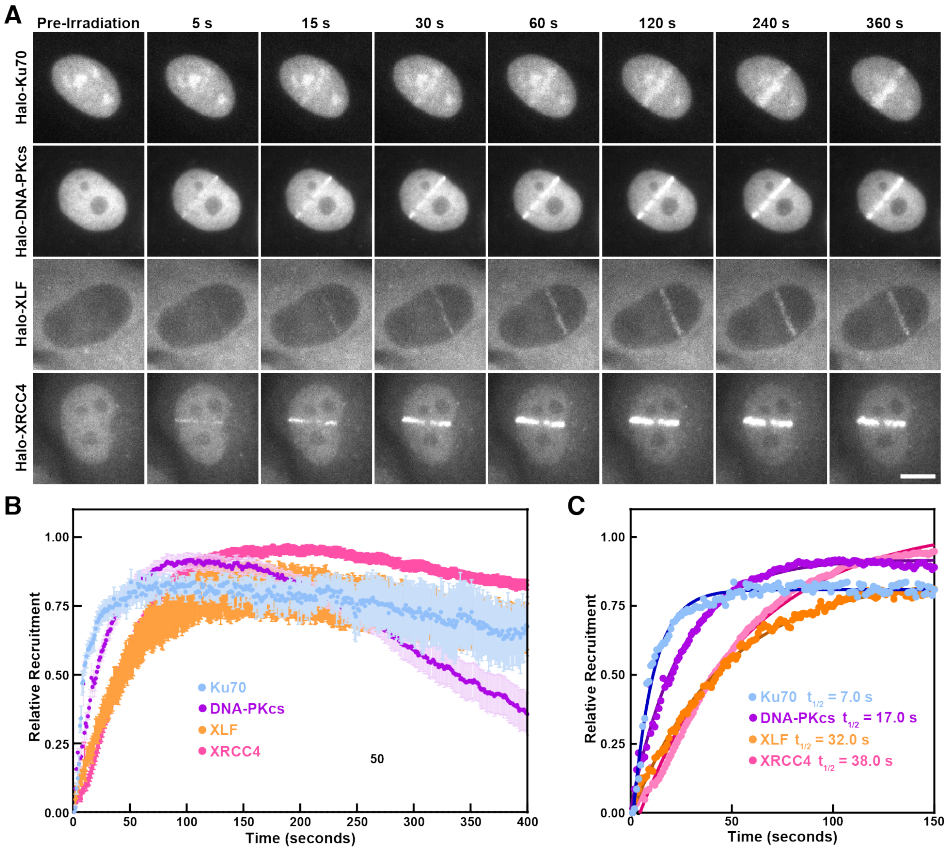

Fig. 2. Recruitment kinetics of the core NHEJ factors to complex DNA lesions A Representative images of HaloTagged NHEJ factor (JFX650) recruitment to laser-induced DNA lesions over time (Scale bar = 10 µm). **B** Normalized recruitment kinetics of HaloTagged DDR proteins to laser-induced DSBs. Data are presented as the average increase in fluorescence post-laser microirradiation normalized to the brightest frame for cell analyzed (N = 10 - 15 individual cells analyzed for each HaloTag cell line, Mean ± S.D.). **C** Half-times ($t_{1/2}$) of each protein to laser-induced DSBs determined by nonlinear regression assuming one-phase association (without dissociation).

cleus (Fig. 1C). In contrast, Halo-XLF was detected in both the cytoplasm and the nucleus. To determine whether the cytoplasmic localization of XLF was an artifact resulting from its fusion with the HaloTag, we performed cellular fractionations of parental U2OS and the Halo-XLF cell line. Both wildtype XLF and Halo-XLF are present in cytoplasm and nucleus (Fig. S1A), demonstrating that XLF cellular localization is not limited to the nucleus in U20S cells. Notably, Halo-DNA-PKcs, Halo-XLF, and Halo-XRCC4 were excluded from nucleoli (Fig. 1C). In contrast, in the absence of DNA damage, Halo-Ku70 was present in both the nucleoplasm and enriched in nucleoli (Fig. 1C). However, in the presence of Zeocin, Halo-Ku70 appeared to be evicted from nucleoli (Fig. 1C), consistent with observations by others [18]. Importantly, none of the NHEJ factors formed DNA repair foci after induction of DSBs using Zeocin, while Rif1 repair foci were readily detectable after DSBs induction, as expected [19]. To assess whether the HaloTag disrupts cellular function of the tagged NHEJ factors, we carried out clonogenic survival assays. Zeocin resistance in the four HaloTagged NHEJ factor cell lines was compared to parental U2OS cells, while DNA-PKcs knock-out cells were highly sensitive to Zeocin (Fig. 1D, Fig. S1B). We conclude that the N-terminal fusion of the 3xFLAG-HaloTag does not significantly alter the DNA repair function of Ku70, DNA-PKcs, XRCC4 or XLF.

Absolute cellular abundance of Ku70, XLF and XRCC4. To determine the absolute cellular abundance of Ku70, XLF, and XRCC4 we compared the fluorescence intensity of labeled Halo-Ku70 and Halo-XRCC4 bands on SDS-PAGE gels to that of a standard containing a known quantity of recombinant 3xFLAG-HaloTag protein labeled with the same fluorophore and a cell lysate from a specified number of cells (Fig. S1C-D). The absolute abundance of Halo-XLF was determined by comparing the fluorescence intensity of Halo-XLF to that of Halo-XRCC4 normalized to total protein loaded (Fig. 1E). To calculate the absolute abundance of endogenous, untagged proteins the absolute abundance of the HaloTagged variants was multiplied by the relative expression of the HaloTagged proteins compared to their untagged counterparts determined by western blot (Fig. 1B). As previously described, the expression level of Ku70 is very high (1.3 - 1.6x10^6 molecules per cell) [20].The expression levels of XLF (54 - 61x10^3 molecules per cell) and XRCC4 (23 - 28x10^3 molecules per cell) were substantially lower. In previous work we determined that DNA-PKcs is present at 120x10^6 molecules per cell [17]. Together these observations demonstrate that the abundance of the core NHEJ factors spans two orders of magnitude, and the components of the initial end-binding complex (Ku70 and DNA-PKcs) are present in at least 10-fold excess over the components of the ligation competent short-range complex (XLF and XRCC4),

taking into account that XRCC4 acts as a dimer and XLF is largely excluded from the nucleus.

Stepwise recruitment of NHEJ factors to laser micro-irradiatation induced DNA lesions. To analyze the recruitment of the tagged NHEJ factors to DNA lesions in real time, we performed laser micro-irradiation (LMI) experiments using a 405 nm laser of cells sensitized with Hoechst dye. While LMI induces complex DNA lesions (and not single DSBs), it provides very consistent experimental conditions (pulse length, laser power) and allows analysis of NHEJ factor localization to DNA lesions with minimal time delay after induction of DNA damage [21]. All tagged NHEJ factors were robustly recruited to LMI-induced damage sites (Fig. 2A-C, Fig. S2A-D, Movie S1-4). Halo-Ku70 and Halo-DNA-PKcs were recruited to damaged sites very rapidly, with a half-maximal accumulation time ($t_{1/2}$) of 7 and 17 seconds, respectively (Fig. 3C, Movie S1-2). Halo-XRCC4 and Halo-XLF were recruited with similar kinetics, but were delayed ($t_{1/2}$ = 32 and 38 s) compared to Halo-Ku70 and Halo-DNA-PKcs, consistent with previous results (Fig. 2A-C, Movie S3-4) [22]. Similar to Zeocin-induced damage, LMI also induces depletion of Halo-Ku70 from nucleoli (Fig. 2A, Movie S1). These observations demonstrate that the HaloTagged NHEJ factors can bind to DNA lesions and the delayed recruitment of XRCC4 and XLF is consistent with the initial formation of an NHEJ complex composed of only Ku70/80 and DNA-PKcs.

Zeocin-induced DSB formation promotes chromatin association of Halo-tagged NHEJ factors. To analyze the diffusion dynamics of individual HaloTagged NHEJ factors, we carried out highly inclined laminated optical sheet (HILO) microscopy of cells sparsely labeled with a fluorescent HaloTag ligand in combination with single-particle tracking (SPT) [23,24]. Under these conditions only a small fraction of the total cellular proteins was labeled, ranging from 0.01% for Halo-Ku70 to 0.6% for Halo-XLF (Fig. S3A-B, Movie S5-7). Analysis of single-molecule trajectories using the Spot-On tool, allowed us to determine the fraction of static molecules, which we presume include molecules that are directly associated with chromatin, including DSBs (Fig. 3A-B) [23]. In addition, Spot-On determines the diffusion coefficients of freely diffusing molecules (D_{Free}) and chromatin bound (D_{Bound}) molecules (Fig. 3B) [23]. As controls for freely diffusing and chromatin bound proteins, constructs encoding only the HaloTag fused to three nuclear localization sequences (Halo-NLS) and HaloTag-histone H2B (Halo-H2B) were transfected into parental U2OS cells [17].

Halo-NLS diffused rapidly through the nucleus (DFree = 2.6 $\mu m^2/s$) and only a small fraction of molecules were static (F_{Bound} = 10%, Fig. 3C-D, Fig. S3D). In contrast and as expected, the majority of Halo-H2B was associated with chromatin (FBound = 80%, Fig. 3C). In the absence of DNA damage, all four HaloTagged NHEJ factors displayed an intermediate level of chromatin bound molecules (FBound = 20-30%, Fig. 3C, Fig. S3D). Upon DNA damage induction the chromatin associated fraction of all tagged NHEJ factors significantly increased by 10-20% (Fig. 3C), demonstrating that this single-molecule imaging approach can detect the recruitment of NHEJ factors to DSBs, even though DNA repair foci specific for the core NHEJ factors are generally not detectable by traditional microscopy. The increase in the chromatin bound fraction of DNA-PKcs correlated with the dose of Zeocin used (Fig. S3C), consistent with the recruitment of DNA-PKcs to chromatin as a consequence of DSBs formation. To confirm that Halo-DNA-PKcs was recruited to chromatin in response to DSB induction in a different cell line, we expressed Halo-DNA-PKcs in CHO-V3 cells (Chinese hamster ovary cells that lack DNA-PKcs). Similar to our observations in U2OS cells, in CHO-V3 cells the chromatin bound fraction of Halo-DNA-PKcs was also increased in response to Zeocin treatment (Fig. S3E). The diffusion coefficients of freely diffusing Halo-Ku70, Halo-DNA-Pkcs, and Halo-XRCC4 were comparable in the absence of DNA damage (D_{Free} = 1.6-1.9 $\mu m^2/s$, Fig. 3D). Halo-XLF diffused more rapidly through the nucleus (D_{Free} = 2.5 $\mu m^2/s$), indicating that it does not constitutively associate with the other NHEJ factors, in particular XRCC4. The diffusion coefficients of freely diffusing and chromatin bound Halo-Ku70, Halo-XRCC4, and Halo-XLF molecules were not affected by DSBs induction using Zeocin (Fig. 3D, Fig. S3F). In contrast, the DFree of Halo-DNA-PKcs was reduced to D_{Free} = 0.7 $\mu m^2/s$ after Zeocin treatment (Fig. 3D). Similarly, the D_{Bound} of of Halo-DNA-PKcs was also reduced after DSB induction (Fig. S3E). This suggests that DNA-PKcs globally transitions into a different macro-molecular complex after DNA damage induction, or it forms many transient interactions with chromatin that slow down its diffusion dynamics.

In addition to defining the diffusion dynamics of the HaloTagged NHEJ factors, these experiments allowed us to estimate the number of chromatin-associated molecules per cell for each of the proteins analyzed. We determined the number of chromatin-bound molecules by multiplying the static fraction with the average number of molecules per imaging frame for each protein. This number was then divided by the labeling efficiency to account for the small fraction of molecules that are detectable. Finally, the resulting number was divided by the number of molecules expected to be present at a single DSB (2 for Ku70 and DNA-PKcs, 4 for XRCC4, 1 for XLF, see Fig. 1A). Assuming the majority of chromatin-bound molecules are associated with DSBs, Halo-Ku70 and DNA-PKcs were associated with 14000 and 5100 DSBs per cell (Fig. S3G), respectively. Halo-XRCC4 and Halo-XLF only associated with 740 and 400 DSBs per cell (Fig. S3G), respectively. These numbers are consistent with the hierarchy of NHEJ factor recruitment, and the relative abundance of the tagged proteins. In addition, these observations suggest that 10,000 DSBs are induced per cell under these experimental conditions.

Altogether, these results demonstrate that single-molecule imaging can be used to study the recruitment of NHEJ factors to DSBs in living cells.

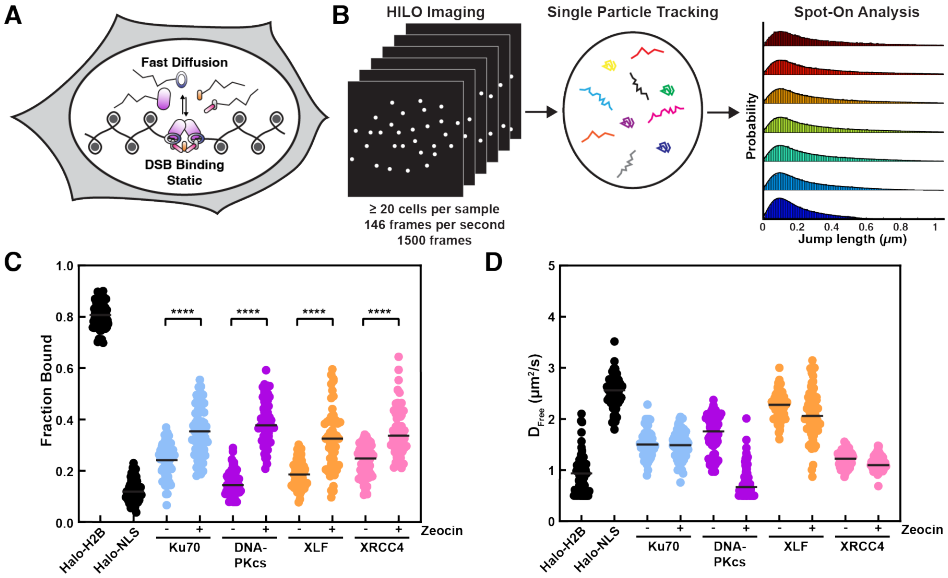

Fig. 3. Zeocin-induced DSB formation promotes chromatin association of Halo-tagged NHEJ factors. A Rational for analyzing DSB association of NHEJ factors using single-molecule imaging. DSB association proteins are static while unbound molecules diffuse rapidly through the nucleus. **B** Graphical representation of the workflow used for live-cell single-molecule imaging of core NHEJ proteins. **C** Plot of the Fraction Bound for each HaloTag NHEJ protein under untreated conditions and post-Zeocin exposure that were analyzed using a two-state model of diffusion. Each data point represents the fraction bound of each protein in an individual cell (N = 3, n 20 cells for each protein per replicate and condition, Black bar = median). Data were analyzed by two-way ANOVA with Tukey's posthoc test (**** = $p < 0.0001$). **D** Diffusion coefficients for freely diffusing HaloTagged NHEJ proteins. Each data point represents the DFree calculated from the tracks in an individual cell (N = 3, n 20 cells for each protein per replicate and condition, Black bar = median).

Single-Molecule Kinetics of NHEJ factor recruitment to Calicheamicin induced DSBs. Next, we used SPT to analyze the kinetics of chromatin association of the HaloTagged NHEJ factors. In this experiment, we used Calicheamicin to induce DSBs with 3' overhangs, a high percentage of which have 3' phospho-glycolate adducts [25,26]. Cultures were treated with 40 nM Calicheamicin for 3 minutes and individual cells were imaged for 10 seconds each before and after damage induction to determine the fraction of chromatin bound molecules (Fig, 4A, each data point represents a different cell). Prior to treatment with Calicheamicin the fraction of chromatin bound molecules remained constant for all NHEJ factors (Fig. 4B). Immediately after DNA damage induction the chromatin bound fraction of Halo-Ku70 and Halo-DNA-PKcs increased (Fig. 4B), consistent with their rapid recruitment to DSBs. Importantly, the fraction bound of Halo-DNA-PKcs cells was not increased after treatment with DMSO (Fig. S4A). The chromatin bound fraction for Halo-XRCC4 and Halo-XLF also increased, but the chromatin recruitment of these factors was delayed by 4 minutes relative to Halo-Ku70 and Halo-DNA-PKcs (Fig. 4B). This suggests that DSBs are initially bound by Ku70/80 and DNA-PKcs, while XRCC4 and XLF are recruited at a later time point, consistent with their delayed association observed using LMI (Fig. 3). Halo-DNA-PKcs dissociated from chromatin 20 minutes after DNA damage induction (Fig. 4B). The rapid drop in the chromatin bound fraction of DNA-PKcs back to baseline levels (those observed before DNA damage induction) suggests that DSBs are repaired synchronously under these experimental conditions. Relative to Halo-DNA-PKcs, Halo-Ku70, Halo-XRCC4, and Halo-XLF remained bound to DSBs for an additional 10 minutes (Fig. 4B), consistent with the formation of the ligation competent short-range synaptic complex that lacks DNA-PKcs.

To determine whether the catalytic activity of DNA-PKcs is required for its dissociation from DSBs and in turn the completion of DNA repair marked by the departure of the other NHEJ factors, the experiment was repeated in the presence of an DNA-PK inhibitor (Nu7441) [27]. When DNA-PKcs kinase activity was inhibited, all four NHEJ factors remained associated with chromatin for >60 minutes (the end of the experiment) when the catalytic activity of DNA-PKcs was inhibited, suggesting that DNA-PKcs target phosphorylation is required for DNA-PKcs displacement from the NHEJ complex and potentially end ligation. To assess whether DNA-PKcs autophosphorylation at the ADCDE-sites, which is important for DNA-PKcs function [10,28–31], is required for its dissociation from DSBs, we expressed wildtype Halo-DNA-PKcs and Halo-DNA-PKcs with the ABCDE sites mutated to alanine (ABCDE mutant) in U2OS cells in which endogenous DNA-PKcs was knocked out. Similar to Halo-DNA-PKcs in the presence of the DNA-PKcs inhibitor, the ABCDE mutant remained associated with chromatin for the entirety of the experiment, while wildtype Halo-DNA-PKcs dissociated from chromatin 20 minutes after DSB induction (Fig. 4D, Fig. S4B). This demonstrates that DNA-PKcs autophosphorylation at the ABCDE sites is critical for its departure from DSBs.

It total, these observations in living cells are consistent with a stepwise maturation of the NHEJ complex at DSBs that requires DNA-PK kinase activity; Ku70/80 and DNA-PKcs initially recognize DSBs and recruit XRCC4 and XLF. DNA-PKcs autophosphorylation-induced dissociation occurs well before repair is complete, while the other core NHEJ

factors remain associated with the break sites, consistent with progression to the short-range synaptic complexes where the final resolution of the DSB occurs.

Discussion

Recent single-molecule FRET and Cryo-EM studies suggest that NHEJ is initiated by the formation of a long-range synaptic complex, which can have two distinct compositions [9–13,15]. The long-range complex transitions into a short-range synaptic complex which allows ligations of the DNA ends in a step that requires DNA-PK kinase activity. While these elegant studies defined critical aspects of the molecular mechanism underlying NHEJ, our knowledge on how NHEJ proceeds in living cells was limited.

Unlike DNA damage response factors, only a small number (one to four) of the core NHEJ factors are recruited to individual DSBs. In combination with their high abundance, detecting the recruitment of NHEJ factors to DNA lesions was therefore not possible using traditional microscopy approaches. To overcome this hurdle, we used single-molecule live-cell imaging to study the kinetics of NHEJ factor recruitment to drug induced DSBs. Our key assumption is that the immobilization of individual NHEJ factors in response to treatment with DNA damaging agents is caused by their binding to DSBs. Our single-molecule approach has two key advantages, it allows us to detect individual molecules, which makes it possible to visualize the recruitment of factors that are not present at breaks in large numbers, and we are able to use small molecule drugs to induce a titratable number of chemically defined DNA lesions, rather than the complex and large number DNA damage sites that result from LMI. Our observations demonstrate that Ku70 and DNA-PKcs are recruited to DSBs immediately after their formation. In contrast the recruitment XRCC4 and presumably its constitutive binding partner Ligase 4, as well as XLF is delayed by 4 minutes relative to Ku70 and DNA-PKcs. This is consistent with an initial formation and potentially DNA end synapsis by the domain-swap Ku70/80-DNA-PKcs dimer, which then recruits XRCC4, Ligase 4, and XLF and transitions into the XLF-mediated dimer. Next, we show that the four core NHEJ factors all remain associated with DSBs for 15 minutes at which point DNA-PKcs dissociates, while Ku70 and the ligase complex remain bound for an additional 10 minutes. We believe the dissociation of DNA-PKcs marks the transition from the long-range synaptic complex to the ligation competent short-range synaptic complex. In total, Ku70, which is bound throughout the entire process, remains bound for ∼30 minutes, suggesting DNA break repair by NHEJ is completed in this time frame in living cells. In addition, the formation of the short-range synaptic complex, takes ∼18 minutes, which is in good agreement with the overall kinetics observed in the single-molecule FRET experiments [15]. Importantly, the dissociation of DNA-PKcs requires the kinase activity of DNA-PK, specifically DNA-PKcs autophosphorylation at the ABCDE sites, as previously suggested [32–34]. Moreover, upon inhibition of DNA-PK catalytic activity all core NHEJ factors remain associated with DSBs, demonstrating that short-range synaptic complex formation requires phosphorylation of a functionally relevant DNA-PK targets including the ABCDE sites, consistent with the FRET studies [15].

An important limitation of our work is that we cannot determine the time point of long-range complex formation. Graham *et al.* reported that NHEJ long-range complexes are short-lived (only a few seconds)' whereas short-range NHEJ complexes are considerably more stable [15]. We suggest that while DNA-PKcs is associated with DNA ends, numerous long-range complexes form at a single DSB in an iterative fashion to facilitate different aspects of end-processing. Although how each DSB is shuttled between different complexes has not been determined, emerging data suggest that DNA-PKcs's unique DNA End Blocking helix, which appears to melt the DNA termini within the DNA-binding cradle, may provide a mechanism for DNA-PK to sample DNA ends so that appropriate NHEJ complexes are formed depending on the end chemistry of the DNA end bound [16]. Once ligatable ends are paired within an XLF-mediated dimer, DNA-PKcs autophosphorylates ABCDE sites in trans, resulting in dissociation of DNA-PKcs and progression to the ligation competent short-range complex. The duration of Ku, XRCC4, and XLF at a DSB after DNA-PKcs dissociation (∼10 minutes in our studies) would be fairly consistent with the persistence of short-range complexes detected by single molecule studies in *Xenopus Laevis* extracts by Graham *et al.* [15]. Because of the induction of breaks occurs during a short time window (3 minutes), synchronous recruitment of the NHEJ factors to DNA breaks was not surprising. In contrast, we did not expect the rapid decrease, in the case of DNA-PKcs precisely 18 minutes after damage induction, in the chromatin bound fraction of the core NHEJ factors. Importantly, the timing of NHEJ factor release and the rapid decrease in their chromatin bound fraction was highly reproducible. These observations suggest that the repair of DSBs occurs synchronously for all breaks within a cell and even across cells, which is consistent with NHEJ being carried out with similar kinetics during different cell cycle stages. In addition, our results demonstrate that only a subset of DSBs are bound by XLF and XRCC4 (<750 per cell), compared to the >5000 DSBs per cell bound by Ku70 and DNA-PKcs. This suggests that the components of the ligase complex and in particular XLF, due to its nuclear exclusion and central position in the NHEJ complex, could be the rate limiting factors that control the overall kinetics and cellular capacity of NHEJ.

Altogether the data presented in this paper demonstrate that in living cells NHEJ occurs in a precisely controlled sequence of compositional changes in the NHEJ complex associated with DSBs, which is strong agreement with previous biochemical and structural studies.

ACKNOWLEDGEMENTS
We would like to thank members of the Schmidt lab for discussions and Luke Lavis (HHMI Janelia Research Campus) for providing HaloTag dyes. This work was supported by grants from the NIH (DP2-GM142307) to J.C.S. and (F32GM139292) to J.R.H.. This preprint was generated using a template from Ricardo Henriques.

AUTHOR CONTRIBUTIONS
Conceptualization: M.M, K.M., and J.C.S.; Experiments: M.M., J.R.H.,K.M.; Data

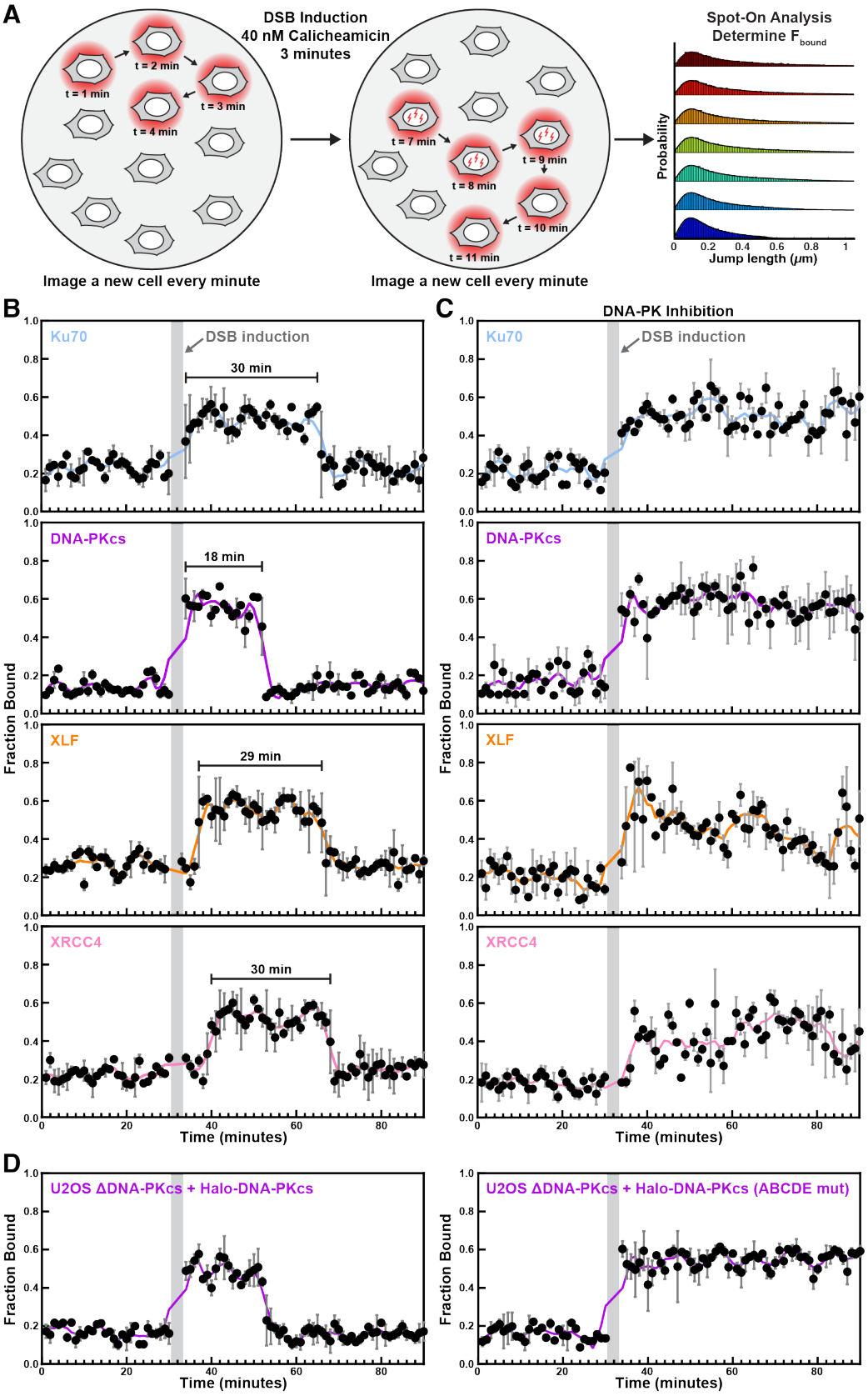

Fig. 4. Kinetics of NHEJ factor association with Calicheamicin induced DSBs A Experimental approach to analyze the chromatin binding of the tagged DNA repair factors over time. **B-C** Plot of the static fraction of each HaloTag NHEJ protein over time **B** in the absence and **C** in the presence of a DNA-PK inhibitor (Nu7441, 100 nM). A single cell was imaged at each timepoint. After 30 minutes DSBs were induced with 40 nM Calicheamicin for 3 minutes (shaded area) and cells were imaged for 60 minutes thereafter (N = 3, Mean ± S.D.). **D** Plot of the static fraction of Halo-DNA-PKcs (left) and Halo-DNA-PKcs (ABCDE mut) over time. A single cell was imaged at each timepoint. After 30 minutes DSBs were induced with 40 nM Calicheamicin for 3 minutes (shaded area) and cells were imaged for 60 minutes thereafter (N = 3, Mean ± S.D.).

Analysis: M.M., J.R.H.; Writing—Original Draft: M.M.; Writing—Review and Editing: M.M., K.M., and J.C.S.

COMPETING INTERESTS
The authors declare no competing interests.

Methods

Cell Lines and Cell Culture. U2OS cells were cultured in RPMI supplemented with 10% fetal bovine serum (FBS), 100 units/mL penicillin, and 100 µg/mL streptomycin. CHO-V3 cells were grown in alpha-MEM containing 10% FBS, 2 mM L-glutamine, 0.1 mM non-essential amino acids, 1 mM sodium pyruvate, 100 U/ml penicillin, 100 µg/ml streptomycin, and 10 µg/ml ciprofloxacin. In addition, stable transfectants of CHO-V3 cell were selected and maintained in complete medium containing 10 µg/ml puromycin. All cells were grown at 37°C in a humidified atmosphere with 5% CO_2.

Molecular Cloning, Plasmids and Genome Editing. Endogenous tagging of Ku70, XLF, and XRCC4 was performed with CRISPR/Cas9 mediated homology-directed repair (HDR) to precisely introduce HaloTag. To achieve this, sgRNAs were inserted into the BbsI site of the pX330 plasmid (pX330-U6-Chimeric-BB-CBh-hSpCas9 was a gift from Feng Zhang, Addgene plasmid Nr. 42230) [35]. Each HDR donors was made up of three inserts: a left homology arm, a right homology arm, and an insertion in-between the homology arms including a 3x FLAG tag, an inverted SV40 promoter, a Puromycin resistance cassette (PuroR) flanked by LoxP sites (for further selection), the HaloTag, and a TEV protease cleavage site, followed by a short peptide linker sequence, as previously described 38. Homology arms were ordered from IDT. U2OS cells were transfected with 1 µg of pX330 plasmid and 1 µg of the HDR donor plasmid using 1 ug FuGene 6 (Promega). Approximately 2-3 days post-transfection, edited cells were selected with 1 ug/mL puromycin. These cells were transfected with 2 µg of plasmid encoding eGFP-Cre recombinase (CAG-GFP-IRES-CRE was a gift from Fred Gage, Addgene plasmid Nr. 48201) [37]. To obtain individual clones, cells that were eGFP and JFX650 positive, were sorted into single wells of 96-well cell culture plates. For knockout of DNA-PKcs, cells were transfected with two gRNA plasmids (TGCAACTTCACTAAGTCCA, GAAAAAGTACATTGAAATT). Knockout was confirmed by Western blot and Sanger sequencing. For transient transfection of wild type Halo- DNA-PKcs and Halo-ABCDE plasmids, 1ug of plasmid and FuGene 6 (Promega) were used. CHO-V3 transfectants expressing human DNA-PKcs were derived by stably transfecting cells with 10 ug expression plasmid and 1 ug pSuper-Puro with PEI. 48 hours after transfection, cells were plated at limiting dilution in media containing 5 ug/ml puromycin. Isolated clones were screened for DNA-PKcs expression by immunoblotting.

Antibodies and immunoblotting. Cell extracts were prepared in 2x Laemmli buffer with beta-mercaptoethanol. Proteins were resolved by SDS–PAGE using Mini-PROTEAN TGX stain-free gels (BioRad), except for DNA-PKcs for which homemade 6% polyacrylamide gels were used. Proteins were transferred to PVDF using either a Trans-Blot Turbo system (with Turbo transfer buffer) (BioRad) or by traditional wet tank transfer using CAPS Buffer with 10% Methanol (for DNA-PKcs). Antibodies used in this study were anti-DNA-PKcs (1:1000 dilution) [38], anti-XLF (Invitrogen PA596310, 1:1000), anti-XRCC4 (Invitrogen, PA5-82264, 1:2000), anti-Ku70 (Invitrogen, MA5-12933, 1:1000), anti-Lamin B1 (Proteintech, 12987-1-AP), and anti-Tubulin (Proteintech, 66031-1-Ig). A chemiluminescence signal was produced using the Clarity western ELC substrate (BioRad) and detected using a ChemiDoc imaging system (BioRad).

Measure and quantifying an in-gel fluorescence and protein abundance. To measure in-gel fluorescence, cells were labeled for 30 minutes with 500 nM JF646 or JFX650 HaloTag ligand. On a BioRad Chemidoc, fluorescence was visualized using the Cy5.5 filter. Total protein was detected using TGX stain free gels (BioRad) and a Chemidoc imager (BioRad) using 45 seconds of UV activation. For in-gel fluorescence quantification of the HaloTagged proteins, we used a previously described method [17,39]. Briefly, we created a standard curve utilizing known amounts of recombinant 3X FLAG-HaloTag labeled with JF646 and cell lysates from a known number of U2OS cells to evaluate protein abundance in two clones for each cell line. To account for the possibility of different expression of HaloTagged proteins relative to untagged proteins, we obtained a western blot correction factor. All in-gel fluorescent SDS-page gels and western blots have at least 3 technical and 3 biological replicates.

Clonogenic Survival Assays. The day before Zeocin treatment, cells were seeded in six-well plates in triplicate at a density of 500 cells per well. The next day, cells were treated using a range Zeocin (Gibco) concentrations for four hours, and then media with drug was substituted with fresh complete media. Approximately 7–10 days after exposure to Zeocin, 6-well plates were rinsed with PBS, and cells were fixed and stained in crystal violet solution (20% ethanol and 1% w/v crystal violet). The crystal violet solution was removed by carefully careful washing with water. Dry plates were imaged using the Coomassie Blue filter set on a BioRad Chemidoc. Colony counts were determined using ImageQuant TL 8.2. All colony survival assays were performed with 4 biological replicates.

Live cell imaging. Live cell imaging was carried out on a Olympus IX83 inverted microscope equipped with a 4-line cellTIRF illuminator (405 nm, 488 nm, 561 nm, 640 nm lasers), an Excelitas X-Cite TURBO LED light source, an Olympus UAPO 100x TIRF objective (1.49 NA), an Olympus UPlanApo 60x TIRF oil-immersion objective (1.50 NA), a CAIRN TwinCam beamsplitter, two Andor iXon Ultra EMCCD cameras or two Hamamatsu Orca BT Fusion cameras, a cellFRAP with a 100 mW 405 nm laser, an environmental control enclosure for temperature, CO_2, and humidity

control. The microscope was operated using the Olympus cellSense software.

Laser Micro-irradiation. Cells were labeled with the Halotag ligand JFX650 (a kind gift from the Lavis lab, Janelia Farms, Ashburn, VA) at a concentration of 500 nM in complete media for 30 min at 37°C, washed three times, and presensitized with Hoechst (1 µg/mL) for ten minutes. The 405-nm laser was directly coupled to the epifluorescence optical path of the microscope with 100x objective and fluorescence imaged with excitement by the 630 nm LED light source at every 1 second. DNA lesions were generated in a straight line across the nucleus by micro-irradiation with the 405-nm laser at 25% laser power using 20 ms pulse. For quantitative analyses, we first cropped cells and drift corrected using NanoJ in Fiji [40]. Intensity profiles of the laser micro-irradiated stripe were generated using ImageJ and data was analyzed using GraphPad Prism by fitting an exponential one-phase association model.

Single-molecule imaging. Cells were grown on 24-well glass bottom dishes (Cellvis, P24-1.5H-N) and imaged after 24h. Cells were sparsely labeled with JFX650 or JF646 dye [41,42] in complete media (Halo-Ku70 100 pM for 30 seconds, Halo-DNA-PKcs 1 nM for 1 minute, Halo-XRCC4 50 nM for 1 minute, Halo-XLF 10 nM for 1 min) and were washed three times with fresh media and incubated for an additional 15 min at 37°C (5% CO_2) to remove excess dye. Cells were treated for one hour prior to HaloTag labeling with 100 ug/mL Zeocin or DMSO and imaged at 146 frames per second for 3000 frames using the Andor 897 Ultra EM-CCD camera. For Calicheamicin treatment, cells were labeled and imaged for 30 minutes prior to adding the 40 nM of drug for 3 minutes while in cellVivo chamber and washed away at least 3 times with complete media. To inhibit DNA-PK, cells were treated with 100 nM Nu7441 for 2 hours prior to and during imaging. Cells for imaged at 179 frames per second for 1500 frames using the Hamamatsu Orca Fusion BT sCMOS camera. All experiments have been done in at least a triplicate with at least 15 cells for each experiment.

Analysis of Live-Cell Imaging. To analyze the single-molecule particles TIFF files, we used the batch parallel-processing version of SLIMFAST in MatLab 2020b [23]. For tracking, the following settings were used for all the proteins: Exposure Time = 5.6 or 6.8 ms, NA = 1.49 or 1.50, PixelSize = 0.16 or 0.1083 µm, Emission Wavelength = 664 nm, Dmax = 5 µm2 s-1, Number of gaps allowed = 2, Localization Error = 10-5, Deflation loops = 0. We only analyzed particles located in nucleus using brigh field images to make a mask of nucleus in ImageJ. Using tracked particles, we determined the diffusion coefficients and the bound fractions using the MATLAB version of SpotOn [23]. The following settings were used: TimeGap = 5.6 or 6.8 ms, dZ = 0.700 µm, GapsAllowed = 2, TimePoints = 8, JumpsToConsider = 4, BinWidth = 0.01 µm, PDFfitting. We applied a 2-state model with the following settings: D-Free2-1State = [0.5 5], D-Bound2-State = [0.0001 0.5] with an assumption that are or chromatin bound or are freely diffusing. To compare Diffusion coefficients and bound fractions, we were performed by two-way ANOVA with Tukey's posthoc test in GraphPad Prism.

Cellular fractionation. Cellular fractionation was performed as previously described [43]. Briefly, 20 million cells were trypsinized, collected, and washed in ice-cold PBS before swelling in a hypotonic buffer (10 mM HEPES pH 7.9, 10 mM KCl, 1.5 mM $MgCl_2$, and 0.5 mM DTT). Then, using a pre-cooled dounce homogenizer and the tight pestle, swollen cells were ruptured with 13 strokes (VWR Cat. 62400-595). The purify the nuclei, burst cells were centrifuged at 218xg for 5 min. To further improve the quality of purified nuclei, the nuclear pellet was resuspended in buffer S1 (0.25 M sucrose, 10 mM $MgCl_2$), layered on top of buffer S2 (0.35 M sucrose, 0.5 mM MgCl2) in a 15 ml falcon tube, and centrifuged at 1430xg in a swinging bucket rotor for 5 min. Nuclei then were resuspended in buffer S2. Samples of each fraction were analyzed by western blot.

References

1. Chapman, J.R., Taylor, M.R.G., and Boulton, S.J. (2012). Playing the End Game: DNA Double-Strand Break Repair Pathway Choice. Mol Cell 47. 10.1016/j.molcel.2012.07.029.

2. Stinson, B.M., and Loparo, J.J. (2021). Repair of DNA Double-Strand Breaks by the Nonhomologous End Joining Pathway. Annu Rev Biochem 90. 10.1146/annurev-biochem-080320-110356.

3. Watanabe, G., and Lieber, M.R. (2023). The flexible and iterative steps within the NHEJ pathway. Prog Biophys Mol Biol 180–181, 105–119. 10.1016/j.pbiomolbio.2023.05.001.

4. Karanam, K., Kafri, R., Loewer, A., and Lahav, G. (2012). Quantitative Live Cell Imaging Reveals a Gradual Shift between DNA Repair Mechanisms and a Maximal Use of HR in Mid S Phase. Mol Cell 47. 10.1016/j.molcel.2012.05.052.

5. Jasin, M., and Rothstein, R. (2013). Repair of strand breaks by homologous recombination. Cold Spring Harb Perspect Biol 5. 10.1101/cshperspect.a012740.

6. Grundy, G.J., Moulding, H.A., Caldecott, K.W., and Rulten, S.L. (2014). One ring to bring them all-The role of Ku in mammalian non-homologous end joining. DNA Repair (Amst) 17. 10.1016/j.dnarep.2014.02.019.

7. Anderson, C.W., and Lees-Miller, S.P. (1992). The nuclear serine/threonine protein kinase DNA-PK. Crit Rev Eukaryot Gene Expr 2.

8. Grundy, G.J., Rulten, S.L., Arribas-Bosacoma, R., Davidson, K., Kozik, Z., Oliver, A.W., Pearl, L.H., and Caldecott, K.W. (2016). The Ku-binding motif is a conserved module for recruitment and stimulation of non-homologous end-joining proteins. Nat Commun 7. 10.1038/ncomms11242.

9. Seif-El-Dahan, M., Kefala-Stavridi, A., Frit, P., Hardwick, S.W., Chirgadze, D.Y., Maia De Oliviera, T., Britton, S., Barboule, N., Bossaert, M., Pandurangan, A.P., et al. (2023). PAXX binding to the NHEJ machinery explains functional redundancy with XLF. Sci Adv 9. 10.1126/sciadv.adg2834.

10. Chen, S., Vogt, A., Lee, L., Naila, T., McKeown, R., Tomkin-

son, A.E., Lees-Miller, S.P., and He, Y. (2023). Cryo-EM visualization of DNA-PKcs structural intermediates in NHEJ. Sci Adv 9, eadg2838. 10.1126/sciadv.adg2838.

11. Chen, S., Lee, L., Naila, T., Fishbain, S., Wang, A., Tomkinson, A.E., Lees-Miller, S.P., and He, Y. (2021). Structural basis of long-range to short-range synaptic transition in NHEJ. Nature 593. 10.1038/s41586-021-03458-7.

12. Chaplin, A.K., Hardwick, S.W., Liang, S., Kefala Stavridi, A., Hnizda, A., Cooper, L.R., De Oliveira, T.M., Chirgadze, D.Y., and Blundell, T.L. (2021). Dimers of DNA-PK create a stage for DNA double-strand break repair. Nat Struct Mol Biol 28. 10.1038/s41594-020-00517-x.

13. Chaplin, A.K., Hardwick, S.W., Stavridi, A.K., Buehl, C.J., Goff, N.J., Ropars, V., Liang, S., De Oliveira, T.M., Chirgadze, D.Y., Meek, K., et al. (2021). Cryo-EM of NHEJ supercomplexes provides insights into DNA repair. Mol Cell 81. 10.1016/j.molcel.2021.07.005.

14. Stinson, B.M., Moreno, A.T., Walter, J.C., and Loparo, J.J. (2020). A Mechanism to Minimize Errors during Non-homologous End Joining. Mol Cell 77. 10.1016/j.molcel.2019.11.018.

15. Graham, T.G.W., Walter, J.C., and Loparo, J.J. (2016). Two-Stage Synapsis of DNA Ends during Non-homologous End Joining. Mol Cell 61. 10.1016/j.molcel.2016.02.010.

16. Buehl, C.J., Goff, N.J., Hardwick, S.W., Gellert, M., Blundell, T.L., Yang, W., Chaplin, A.K., and Meek, K. (2023). Two distinct long-range synaptic complexes promote different aspects of end processing prior to repair of DNA breaks by non-homologous end joining. Mol Cell 83. 10.1016/j.molcel.2023.01.012.

17. Heyza, J.R., Mikhova, M., Bahl, A., Broadbent, D., and Schmidt, J.C. (2023). Systematic analysis of the molecular and biophysical properties of key DNA damage response factors. Elife 12. 10.7554/eLife.87086.

18. Schellenbauer, A., Guilly, M.N., Grall, R., Le Bars, R., Paget, V., Kortulewski, T., Sutcu, H., Mathé, C., Hullo, M., Biard, D., et al. (2021). Phospho-Ku70 induced by DNA damage interacts with RNA Pol II and promotes the formation of phospho-53BP1 foci to ensure optimal cNHEJ. Nucleic Acids Res 49. 10.1093/nar/gkab980.

19. Bekker-Jensen, S., Lukas, C., Kitagawa, R., Melander, F., Kastan, M.B., Bartek, J., and Lukas, J. (2006). Spatial organization of the mammalian genome surveillance machinery in response to DNA strand breaks. Journal of Cell Biology 173. 10.1083/jcb.200510130.

20. Mimori, T., Hardin, J.A., and Steitz, J.A. (1986). Characterization of the DNA-binding protein antigen Ku recognized by autoantibodies from patients with rheumatic disorders. Journal of Biological Chemistry 261, 2274–2278. 10.1016/S0021-9258(17)35929-X.

21. Los, G. V., Encell, L.P., McDougall, M.G., Hartzell, D.D., Karassina, N., Zimprich, C., Wood, M.G., Learish, R., Ohana, R.F., Urh, M., et al. (2008). HaloTag: A novel protein labeling technology for cell imaging and protein analysis. ACS Chem Biol 3. 10.1021/cb800025k.

22. Yano, K., Morotomi-Yano, K., Wang, S., Uematsu, N., Lee, K., Asaithamby, A., Weterings, E., and Chen, D.J. (2008). Ku recruits XLF to DNA double-strand breaks. EMBO Rep 9, 91–96. 10.1038/sj.embor.7401137.

23. Hansen, A.S., Woringer, M., Grimm, J.B., Lavis, L.D., Tjian, R., and Darzacq, X. (2018). Robust model-based analysis of single-particle tracking experiments with spot-on. Elife 7. 10.7554/eLife.33125.

24. Tokunaga, M., Imamoto, N., and Sakata-Sogawa, K. (2008). Highly inclined thin illumination enables clear single-molecule imaging in cells. Nat Methods 5, 159–161. 10.1038/nmeth1171.

25. Dedon, P.C., and Goldberg, I.H. (1992). Free-radical mechanisms involved in the formation of sequence-dependent bistranded DNA lesions by the antitumor antibiotics bleomycin, neocarzinostatin, and calicheamicin. Chem Res Toxicol 5, 311–332. 10.1021/tx00027a001.

26. Menon, V., and Povirk, L.F. (2016). End-processing nucleases and phosphodiesterases: An elite supporting cast for the non-homologous end joining pathway of DNA double-strand break repair. DNA Repair (Amst) 43, 57–68. 10.1016/j.dnarep.2016.05.011.

27. Leahy, J.J.J., Golding, B.T., Griffin, R.J., Hardcastle, I.R., Richardson, C., Rigoreau, L., and Smith, G.C.M. (2004). Identification of a highly potent and selective DNA-dependent protein kinase (DNA-PK) inhibitor (NU7441) by screening of chromenone libraries. Bioorg Med Chem Lett 14, 6083–6087. 10.1016/j.bmcl.2004.09.060.

28. Cui, X., Yu, Y., Gupta, S., Cho, Y.-M., Lees-Miller, S.P., and Meek, K. (2005). Autophosphorylation of DNA-dependent protein kinase regulates DNA end processing and may also alter double-strand break repair pathway choice. Mol Cell Biol 25, 10842–10852. 10.1128/MCB.25.24.10842-10852.2005.

29. Ding, Q., Reddy, Y.V.R., Wang, W., Woods, T., Douglas, P., Ramsden, D.A., Lees-Miller, S.P., and Meek, K. (2003). Autophosphorylation of the catalytic subunit of the DNA-dependent protein kinase is required for efficient end processing during DNA double-strand break r

30. Goodarzi, A.A., Yu, Y., Riballo, E., Douglas, P., Walker, S.A., Ye, R., Härer, C., Marchetti, C., Morrice, N., Jeggo, P.A., et al. (2006). DNA-PK autophosphorylation facilitates Artemis endonuclease activity. EMBO J 25, 3880–3889. 10.1038/sj.emboj.7601255.

31. Liu, L., Chen, X., Li, J., Wang, H., Buehl, C.J., Goff, N.J., Meek, K., Yang, W., and Gellert, M. (2022). Autophosphorylation transforms DNA-PK from protecting to processing DNA ends. Mol Cell 82, 177-189.e4. 10.1016/j.molcel.2021.11.025.

32. Chan, D.W., and Lees-Miller, S.P. (1996). The DNA-dependent protein kinase is inactivated by autophosphorylation of the catalytic subunit. J Biol Chem 271, 8936–8941. 10.1074/jbc.271.15.8936.

33. Reddy, Y.V.R., Ding, Q., Lees-Miller, S.P., Meek, K., and Ramsden, D.A. (2004). Non-homologous end joining requires that the DNA-PK complex undergo an autophosphorylation-dependent rearrangement at DNA ends. J Biol Chem 279, 39408–39413. 10.1074/jbc.M406432200.

34. Block, W.D., Yu, Y., Merkle, D., Gifford, J.L., Ding, Q., Meek, K., and Lees-Miller, S.P. (2004). Autophosphorylation-dependent remodeling of the DNA-dependent protein kinase catalytic subunit regulates ligation of DNA ends. Nucleic Acids Res 32, 4351–4357. 10.1093/nar/gkh761.

35. Cong, L., Ran, F.A., Cox, D., Lin, S., Barretto, R., Habib, N., Hsu, P.D., Wu, X., Jiang, W., Marraffini, L.A., et al. (2013). Multiplex Genome Engineering Using CRISPR/Cas Systems. Science (1979) 339, 819–823. 10.1126/science.1231143.

36. Xi, L., Schmidt, J.C., Zaug, A.J., Ascarrunz, D.R., and Cech, T.R. (2015). A novel two-step genome editing strategy with CRISPR-Cas9 provides new insights into telomerase action and TERT gene expression. Genome Biol 16, 231. 10.1186/s13059-015-0791-1.

37. Zhao, C., Teng, E.M., Summers, R.G., Ming, G., and Gage, F.H. (2006). Distinct Morphological Stages of Dentate Granule Neuron Maturation in the Adult Mouse Hippocampus. The Journal of Neuroscience 26, 3–11. 10.1523/JNEUROSCI.3648-05.2006.

38. Neal, J.A., Xu, Y., Abe, M., Hendrickson, E., and Meek, K. (2016). Restoration of ATM Expression in DNA-PKcs-Deficient Cells Inhibits Signal End Joining. J Immunol 196, 3032–3042. 10.4049/jimmunol.1501654.

39. Broadbent, D.G., Barnaba, C., Perez, G.I., and Schmidt, J.C. (2023). Quantitative analysis of autophagy reveals the role of ATG9 and ATG2 in autophagosome formation. Journal of Cell Biology 222. 10.1083/jcb.202210078.

40. Laine, R.F., Tosheva, K.L., Gustafsson, N., Gray, R.D.M., Almada, P., Albrecht, D., Risa, G.T., Hurtig, F., Lindås, A.C., Baum, B., et al. (2019). NanoJ: A high-performance open-source super-resolution microscopy toolbox. J Phys D Appl Phys 52. 10.1088/1361-6463/ab0261.

41. Grimm, J.B., English, B.P., Chen, J., Slaughter, J.P., Zhang, Z., Revyakin, A., Patel, R., Macklin, J.J., Normanno, D., Singer, R.H., et al. (2015). A general method to improve fluorophores for live-cell and single-molecule microscopy. Nat Methods 12. 10.1038/nmeth.3256.

42. Grimm, J.B., Xie, L., Casler, J.C., Patel, R., Tkachuk, A.N., Falco, N., Choi, H., Lippincott-Schwartz, J., Brown, T.A., Glick, B.S., et al. (2021). A General Method to Improve Fluorophores Using Deuterated Auxochromes. JACS Au 1. 10.1021/jacsau.1c00006.

43. Klump, B.M., Perez, G.I., Patrick, E.M., Adams-Boone, K., Cohen, S.B., Han, L., Yu, K., and Schmidt, J.C. (2023). TCAB1 prevents nucleolar accumulation of the telomerase RNA to facilitate telomerase assembly. Cell Rep 42, 112577. 10.1016/j.celrep.2023.112577.

44. Deo, C., Abdelfattah, A.S., Bhargava, H.K., Berro, A.J., Falco, N., Farrants, H., Moeyaert, B., Chupanova, M., Lavis, L.D., and Schreiter, E.R. (2021). The HaloTag as a general scaffold for far-red tunable chemigenetic indicators. Nat Chem Biol 17, 718–723. 10.1038/s41589-021-00775-w.

Supplementary Movie Legends

Movie S1. Representative movie demonstrating recruitment of JFX650-labeled 3xFLAG-HaloTagged Ku70 to DNA DSBs after laser microirradiation. Images were acquired at one frame per second.

Movie S2. Representative movie demonstrating recruitment of JFX650-labeled 3xFLAG-HaloTagged-DNA-PKcs to DNA DSBs after laser microirradiation. Images were acquired at one frame per second.

Movie S3. Representative movie demonstrating recruitment of JFX650-labeled 3xFLAG-HaloTagged XRCC4 to DNA DSBs after laser microirradiation. Images were acquired at one frame per second.

Movie S4. Representative movie demonstrating recruitment of JFX650-labeled 3xFLAG-HaloTagged XLF to DNA DSBs after laser microirradiation. Images were acquired at one frame per second.

Movie S5. Representative live-cell single-molecule imaging movie of Halo-NLS transiently expressed in U2OS cells, labeled with JFX650, and acquired at 179 frames per second using the Hamamatsu ORCU Fusion BT camera.

Movie S6. Representative live-cell single-molecule imaging movie of Halo-H2B transiently expressed in U2OS cells, labeled with JFX650, and acquired at 179 frames per second using the Hamamatsu ORCU Fusion BT camera.

Movie S7. Representative live-cell single-molecule imaging movie of 3xFLAG-HaloTagged Ku70 in a control cell (left) and a cell treated with zeocin (right), labeled with JFX650, and acquired at 146 frames per second using the Andor 897 Ultra camera.

Movie S8. Representative live-cell single-molecule imaging movie of 3xFLAG-HaloTagged XLF in a control cell (left) and a cell treated with zeocin (right), labeled with JFX650, and acquired at 146 frames per second using the Andor 897 Ultra camera.

Movie S9. Representative live-cell single-molecule imaging movie of 3xFLAG-HaloTagged XRCC4 in a control cell (left) and a cell treated with zeocin (right), labeled with JFX650, and acquired at 146 frames per second using the Andor 897 Ultra camera.

Movie S10. Representative live-cell single-molecule imaging movies of 3xFLAG-HaloTagged DNA-PKcs labeled with JFX650 before and after treatment with Calicheamicin, acquired at 179 frames per second using the Hamamatsu ORCU Fusion BT camera.

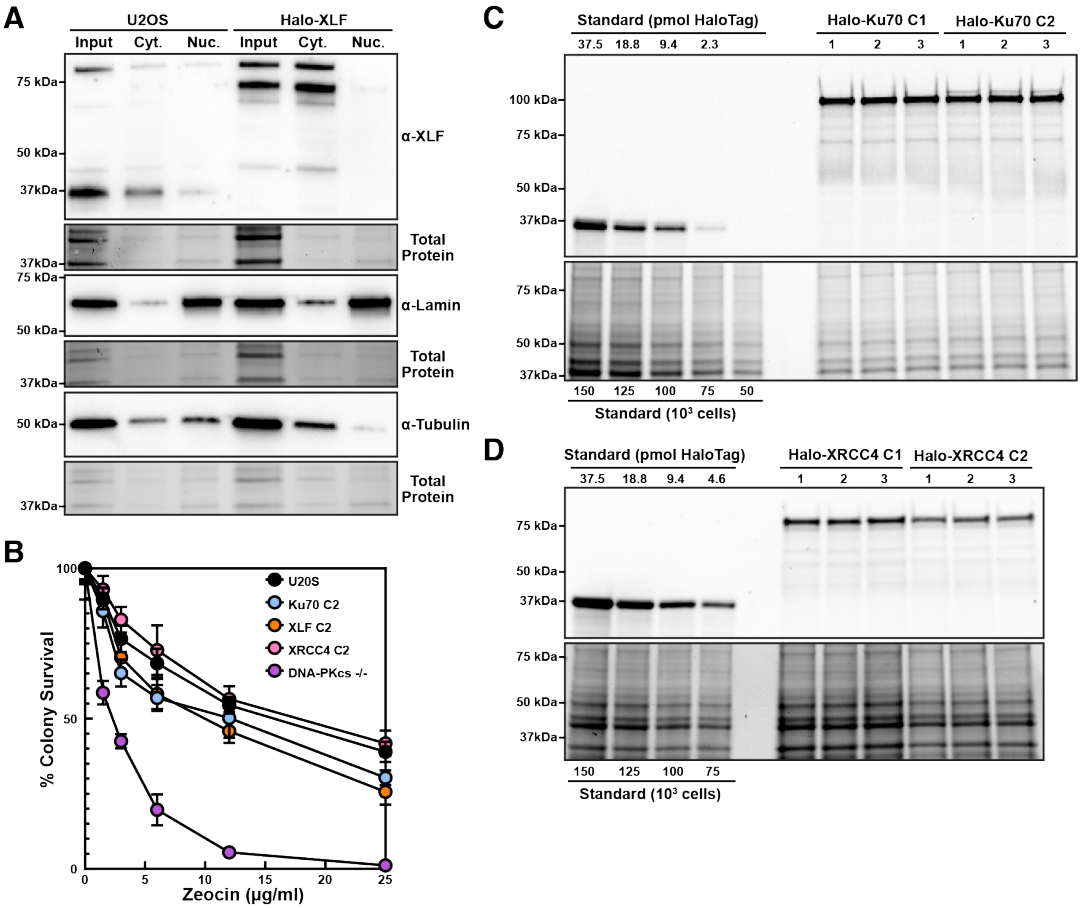

Supplemental Figure 1. Analysis of sub-cellular localization, functionality, and total abundance of HaloTagged DNA repair factors. A Western blot analysis of cytoplasmic (Cyt.) and nuclear (Nuc.) fractions from parental U20S and Halo-XLF cells probed with antibodies against XLF, Lamin (nuclear marker), and Tubulin (cytoplasmic marker). **B** Clonogenic survival assay of of a second independent clone of for all U2OS cells expressing HaloTagged NHEJ factors, parental U2OS cells, and U2OS cells with DNA-PKcs knockout after challenge with Zeocin (N = 4, 3 technical replicates per biological replicate, Mean ± S.D.). **C-D** Fluorescence imaging (JF646) and total protein staining for two clones of **C** Halo-Ku70 and **D** Halo-XRCC4 expressing cells, alongside a protein standard containing a known amount of recombinant 3xFLAG-HaloTag protein labeled with JF646 and whole cell lysate of a known number of cells.

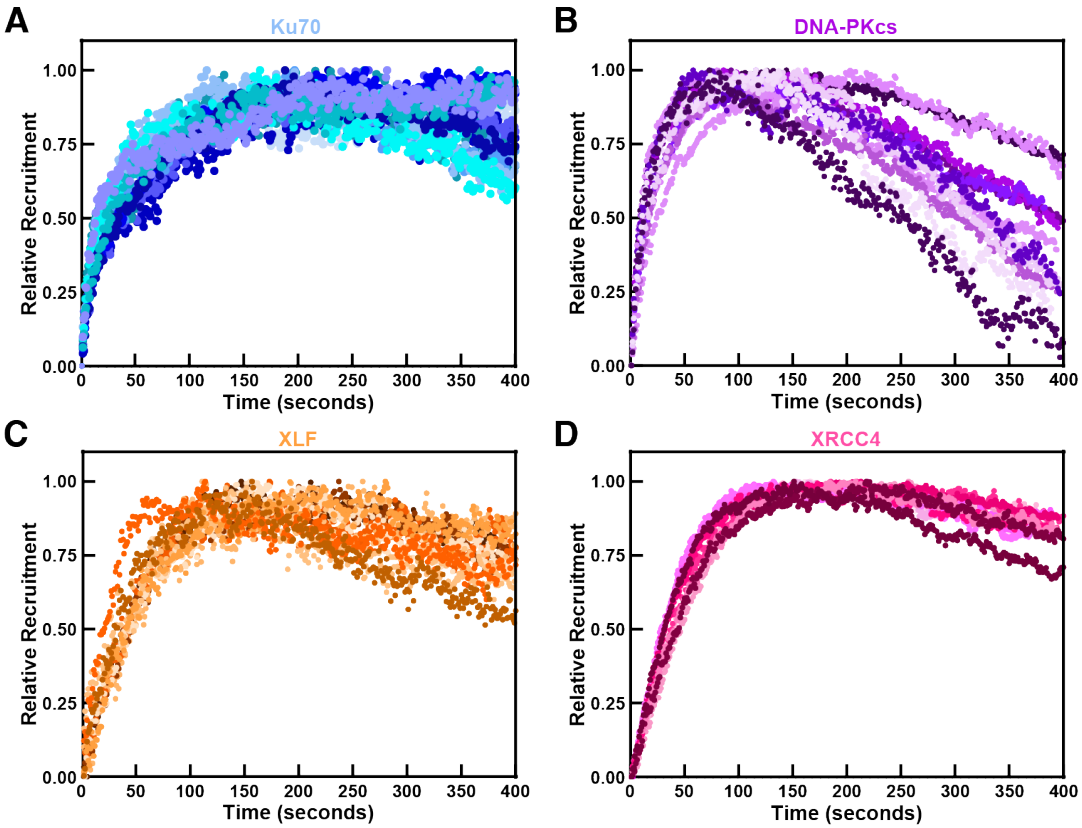

Supplemental Figure 2. Analysis of HaloTagged NHEJ factor recruitment to LMI induced DNA lesions. A-D Plots showing normalized fluorescence intensity and recruitment of **A** Halo-Ku70, **B** Halo-DNA-PKcs, **C** Halo-XLF, and **D** Halo-XRCC4 to laser-induced DNA lesions. Each shade represents data from an individual cell that was analyzed, and the fluorescence intensity was normalized to the brightest frame of each accumulation curve.

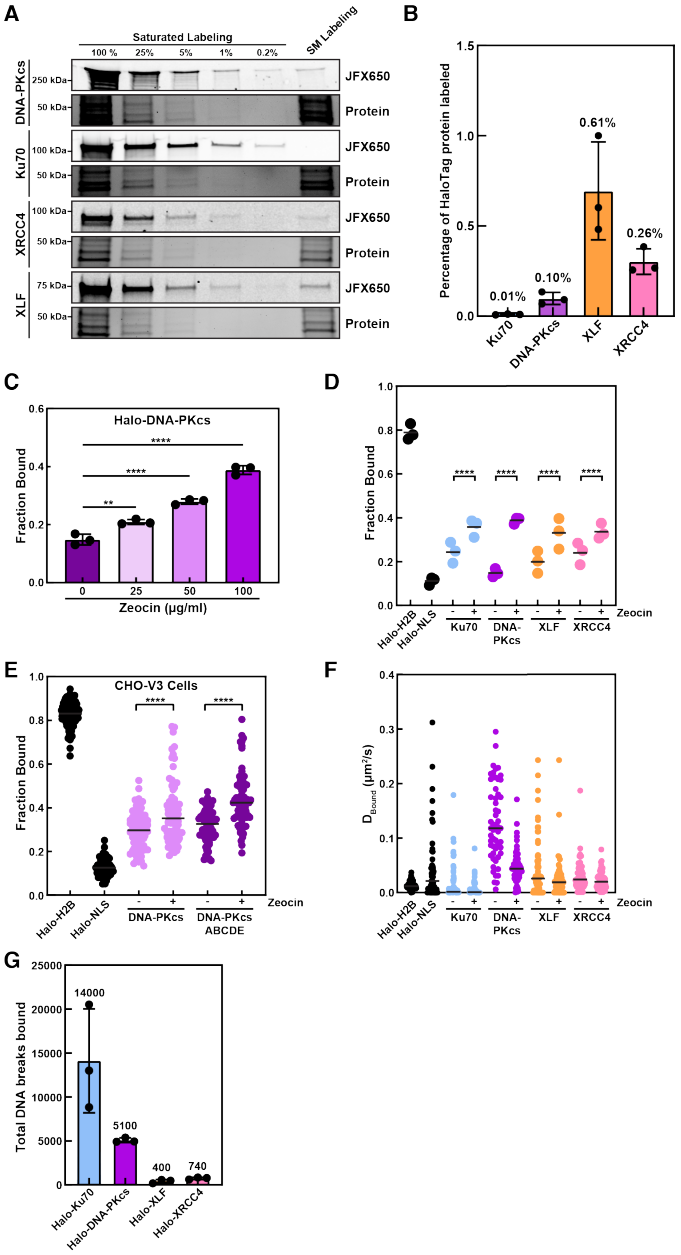

Supplemental Figure 3. Labeling analysis and single-particle tracking of HaloTagged NHEJ factors. A Fluorescence imaging and total protein staining of an SDS-PAGE gel with a standard of each HaloTagged NHEJ factor after labeling under saturation conditions (30 minutes, 100 nM HaloTag ligand) or partial labeling for single-molecule imaging (30 seconds for Halo-Ku70, 1 minute for Halo-DNA-PKcs, Halo-XRCC4, and Halo-XLF, 10 nM HaloTag ligand) with JFX650 HaloTag ligand. **B** Quantification of the fluorescence intensity normalized to total protein loading for the gels shown in **A** (Mean ± S.D.). **C** Fraction bound of Halo-DNA-PKcs in the presence of increasing amounts of zeocin. Each data point represents the Spot-On fit of the pooled data from all cells in a biological replicate (N = 3, n 20 cells for each protein per replicate and condition, Black bar = median). Data were analyzed by two-way ANOVA with Tukey's posthoc test (** = $p < 0.01$, **** = $p < 0.0001$). **D** Plot of the Fraction Bound for each HaloTag NHEJ protein under untreated conditions and post-Zeocin exposure that were analyzed using a two-state model of diffusion. Each data point represents pooled data from all cells in a biological replicate. (N = 3, n 20 cells for each protein per replicate and condition, Black bar = median). Data were analyzed by two-way ANOVA with Tukey's posthoc test (**** = $p < 0.0001$). **E** Plot of the Fraction Bound for Halo-DNA-PKcs wild type and Halo-DNA-PKcs ABCDE mutant transiently expressed in CHO-V3 cells under untreated conditions and post-Zeocin exposure that were analyzed using a two-state model of diffusion. Each dot represents the fraction bound of each protein in an individual cell (N = 3, n 20 cells for each protein per replicate and condition, Black bar = median). Data were analyzed by two-way ANOVA with Tukey's posthoc test (**** = $p < 0.0001$). **F** Diffusion coefficients of static molecules of HaloTag DDR proteins. Each data point represents the D_{Bound} calculated from the tracks in an individual cell (N = 3, n 20 cells for each protein per replicate and condition, Black bar = median). **G** Total number of DNA breaks bound be each tagged DNA repair factor after treatment with zeocin, calculated by multiplying the average particles detected in each imaging frame by the fraction of bound particles divided by the labeling efficiency shown in **B**.

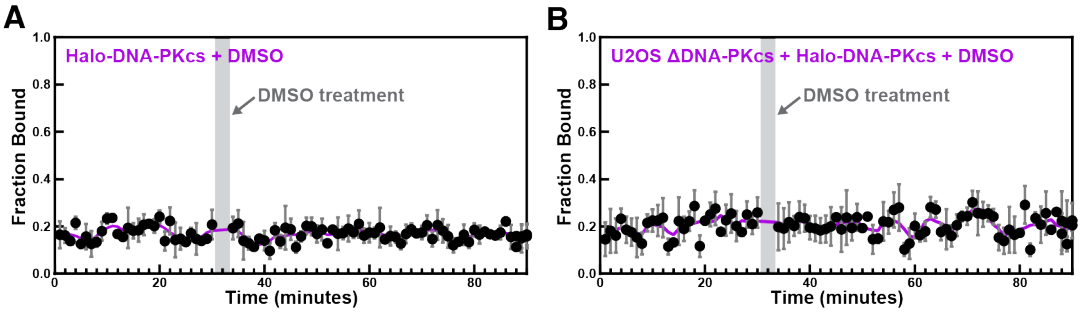

Supplemental Figure 4. Kinetics of chromatin recruitment of Halo-DNA-PKcs under control conditions. A-B Plot of the static fraction of Halo-DNA-PKcs treated with DMSO as a control over time **A** in genome edited U2OS cells expressing Halo-DNA-PKcs from its endogenous locus and **B** in U2OS cells with endogenous DNA-PKcs knocked out Halo-DNA-PKcs expressed by stable transfection (N = 3, Mean ± S.D.).

REAGENT or RESOURCE	SOURCE	IDENTIFIER
Antibodies		
anti-Ku70 polyclonal antibody	Invitrogen	PA596310
anti-DNA-PKcs polyclonal antibody	Neal et al. 2016	N/A
anti-XLF rabbit polyclonal antibody	Invitrogen	111
anti-XRCC4 rabbit polyclonal antibody	Invitrogen	PA5-82264
anti-Tubulin mouse monoclonal antibody	Proteintech	66031-1-Ig
anti-Lamin B1 rabbit polyclonal antibody	Proteintech	12987-1-AP
anti-Mouse HRP	Invitrogen	A-31430
anti-Rabbit HRP	Invitrogen	A-31460
Chemicals, Peptides, and Recombinant Proteins		
JF646 HaloTag Ligand	Grimm et al., 2015	N/A
JFX650 HaloTag Ligand	Grimm et al., 2021	N/A
Zeocin™	Invitrogen	R25001
Calicheamicin	Thermo Fisher	50-202-9283
Puromycin 10 mg/ml	Gibco	A1113803
Lipofectamine 3000	Invitrogen	L3000001
FuGENE® 6 Transfection Reagent	Promega	E2691
Agarose	Fisher Bioreagents	BP1356-500
RPMI Medium 1640 (1x)	Gibco	11875-093
MEM Alpha (1X)	Gibco	12561-049
DPBS (1x)	Gibco	14190-144
Dimethyl Sulfoxide	Fisher Chemicals	D128-500
Research Grade Fetal Bovine Serum	Fisher Chemicals	FB12999102
HOECHST 33342	Invitrogen	62249
2-Mercaptoethanol	Fisher Chemicals	60-24-2
2X Laemmli Sample Buffer	Bio-Rad	1610737
SuperSignal West Femto Maximum Sensitivity Substrate	Thermo Scientific	34096
Clarity Western ECL substrate	Bio-Rad	1705061
Experimental Models: Cell Lines		
U20S, DNA-PKcs KO	This paper	N/A
U20S, FLAG-HaloTag-Ku70 WT	This paper	N/A
U20S, FLAG-HaloTag-DNA-PKcs-WT	Heyza et al. 2023	N/A
U20S, FLAG-HaloTag-XLF WT	This paper	N/A
U20S, FLAG-HaloTag-XRCC4 WT	This paper	N/A
V3, FLAG-HaloTag-DNA-PKcs WT	This paper	N/A
V3, FLAG-HaloTag-DNA-PKcs ABCDE	This paper	N/A
Oligonucleotides		
Ku70 FW primer actcgagaccacgctccttc	This paper	N/A
Ku70 RV primer cgtggaggctatagtgaggg	This paper	N/A
XLF sgRNA CACCGtttttttgcagATGGAAGAAC	This paper	N/A
XLF sgRNA AAACGTTCTTCCATctgcaaaaaaC	This paper	N/A

XRCC4 sgRNA CACCGtttttttgcagATGGAAGAAC	This paper	N/A
XRCC4 sgRNA AAACCCTTGTTTCTGAACCCAGTAC	This paper	N/A
Ku70 gRNA CACCGGAGCAGTAGCCAACATGTCA	This paper	N/A
Ku70 gRNA AAACTGACATGTTGGCTACTGCTCc	This paper	N/A
XRCC4 FW primer CCAGGTCATTCTCACAAGTTCTTGC	This paper	N/A
XRCC4 RV primer CAGCCAAGATCCTAAATGTGGGTG	This paper	N/A
XLF FW primer CCCTGAGAGTTGGATAGCTGT	This paper	N/A
XLF RV primer CTGCCTTGGGCAAGATTAAATCAC	This paper	N/A
XLF LHA CATAAAATGAATGCAATTGTTGTTGTTtgacactatgactta tgatgttttataagacaagaactattccttctcttctagttctgggaaaggatag gagtgacatatttattaggaatgtgataaagatggaacaagaagggtttagg tttccacgttatgttatagtattagaaagcagaaatactaacagcaatatgctg aggtttaaacactatggaagaaagattttctgtcctctaggaatgtaatatggg aaaaaaaaaaccctcaagattttaaatatacttttagtggccaggaggtagt aaagtcagtgctcagctggttgtatactgggagaacgtaaatccatgccttct attttatcagggaggattttcatgagattttagttgatacagactggtttgggtggt gccctccctaggccagcatgaccctgaggctctttactaaatgaggactttttt gcagatgGACTACAAAGACCATGAC	This paper	N/A
XLF RHA CGCGATCGCTTCCggtaccGAAGAACTCGAGCAAGGC CTGTTGATGCAGCCATGGGCGTGGCTACAGCTTGC AGAGAACTCCCTCTTGGCCAAGGTTTTTATCACCAA GCAGGGCTATGCCTTGTTGGTTTCAGATCTTCAACA GGTGTGGCATGAACAGGTGGACACTAGTGTGGTCA GCCAGCGAGCCAAGgtaagtatgaggagaagtactgctgtgtcgg ggatgtgaacatcaaccagcttgctggcctgtagtttcccaaggaaggttga atcgggttgagacaattccagttaatgtcctgtacttctacctgtacttctgcctg gaatcttAACTTGTTTATTGCAGCTTATAATG	This paper	N/A
XRCC4 LHA CATAAAATGAATGCAATTGTTGTTGTTttttagtagagacgg ggtttcaccatgttggccagactggtcttgaactcctgacctcaggcaatctgc ccgtcttggcctcccaaagtgctgggattaccggtgtgagacaccgcgccc agctgagatgataatttttatcttcattacttggacaaatcattttccatttatgggc ctctgcttttctcatctgtaaaaattgtgaattaatattgaagaaaactgtgaattt actgaatgtattatttactgaatttaatggttgaatctaatggttgaacctattata cagtttttttgttttgcttattttcttatttccttggtgtttgtgtagctgagaggccagt acagaaaacattatttgagttacagtttcttttaaaaatattaattgtattctccca ttacagGTATTAAGAAatgGACTACAAAGACCATGAC	This paper	N/A

XRCC4 RHA CGCGATCGCTTCCggtaccGAGAGAAAAATAAGCAGA ATACACCTTGTTTCTGAACCCAGTATAACTCATTTTC TACAAGTATCTTGGGAGAAAACACTGGAATCTGGTT TTGTTATTACACTTACTGATGGTCATTCAGCATGGAC TGGGACAGgtaatactaaaaacaaagtttttataagtaaaatttaagtgt gctattcttcagtcctcagggatacttttccattagatattgggtaaaactgatatt aattttacttgctattgctgtcaaatttatacacaggtttgtaatatttaatgccactt tctatatttaatagtaatagaaaaacaaacgtgtcctagaaaattccggttacc atttgaatcttagtaacttggatttgttcagaggtttaaaatgacctctttatagaa aatataaatagtactttctaaatacatcttttctcaggaccccagAACTTGT TTATTGCAGCTTATAATG	This paper	N/A
3xFlag-Halo ATGGACTACAAAGACCATGACggtgattataaagatcatgatat cgattacaaggatgacgatgacaagggttccatggcagaaatcggtactgg ctttccattcgacccccattatgtggaagtcctgggcgagcgcatgcactacg tcgatgttggtccgcgcgatggcacccctgtgctgttcctgcacggtaacccg acctcctcctacgtgtggcgcaacatcatcccgcatgttgcaccgacccatc gctgcattgctccagacctgatcggtatgggcaaatccgacaaaccagacc tgggttatttcttcgacgaccacgtccgcttcatggatgccttcatcgaagccct gggtctggaagaggtcgtcctggtcattcacgactggggctccgctctgggtt tccactgggccaagcgcaatccagagcgcgtcaaaggtattgcatttatgg agttcatccgccctatcccgacctgggacgaatggccagaatttgcccgcg agaccttccaggccttccgcaccaccgacgtcggccgcaagctgatcatcg atcagaacgtttttatcgagggtacgctgccgatgggtgtcgtccgcccgctg actgaagtcgagatggaccattaccgcgagccgttcctgaatcctgttgacc gcgagccactgtggcgcttcccaaacgagctgccaatcgccggtgagcca gcgaacatcgtcgcgctggtcgaagaatacatggactggctgcaccagtcc cctgtcccgaagctgctgttctggggcaccccaggcgttctgatcccaccgg ccgaagccgctcgcctggccaaaagcctgcctaactgcaaggctgtggac atcggcccgggtctgaatctgctgcaagaagacaacccggacctgatcgg cagcgagatcgcgcgctggctgtcGACGCTCGAGATTTCCGG CgagccaaccactgaggatctgtactttcagagCGATAACGCGAT CGCTTCCGGTACC	Schmidt et. al 2016	N/A
Recombinant DNA		
pHTN HaloTag® CMV-neo	Promega	G7721
pFastBac1	Life Technologies	10360014
pX330	Cong et al., 2013	Addgene: 42230
pmaxGFP	Lonza	Control from Kits
CAG-GFP-IRES-CRE	Addgene	48201
Software and Algorithms		
MATLAB 2019a	Mathworks Inc., USA	http://mathworks.com
ParallelProcess_fastSPT_JF646.m	Hansen et al. 2018	https://github.com/elifesciences-publications/SPT_LocAndTrack
ImageQuant TL 8.2	Cytiva	cytivalifesciences.com

Spot-On	Hansen et al. 2018	https://github.com/elifesciences-publications/spot-on-matlab
Other		
Orange G loading dye (6x), glycerol based	Alfa Aesar	J60562
E.Z.N.A.® Plasmid DNA Maxi Kit	OMEGA Bio-Tek	D6922-02
DNeasy Blood & Tissue Kit (250)	Qiagen	69506
Immobilon® - FL Transfer Membrane	Millipore	IPFL00010
4-15% Mini-PROTEAN TGX precast protein gels	Bio-Rad	4561083
Trans-Blot Turbo RTA Mini 0.2 µm Nitrocellulose Kit	Bio-Rad	1704270
Trans-Blot Turbo 5x Transfer Buffer	Bio-Rad	10026938
24 well Glass Bottom Plate (o.17±0.005 mm)	Cellvis	P24-1.5H-N
SYBR™ Safe DNA Gel Stain	Invitrogen	